International Journal of Technology 15(1) 8-17 (2024)
Received November 2022 / Revised May 2023 / Accepted July 2023

International Journal of Technology

http://ijtech.eng.ui.ac.id

Improved Color Uniformity In White Light-Emitting Diodes Using $LiLu(MoO_4)_2:Sm^{3+}$ Combined SiO_2 Composite

Ha Thanh Tung[1], My Hanh Nguyen Thi[2], Nguyen Doan Quoc Anh[3*]

[1]*Faculty of Basic Sciences, Vinh Long University of Technology Education, Vinh Long Province, Vietnam*
[2]*Faculty of Mechanical Engineering, Industrial University of Ho Chi Minh City, Ho Chi Minh City, Viet Nam*
[3]*Faculty of Electrical and Electronics Engineering, Ton Duc Thang University, Ho Chi Minh City, Vietnam*

Abstract. The research herein concerns the composite of red phosphor of $LiLu(MoO_4)_2:Sm^{3+}$ (LMOS), yellow phosphor $YAG:Ce^{3+}$, SiO_2 particles, and silicone gel. The LMOS phosphor is created via the sol-gel procedure and supposed to yields significant heat consistency. The concentration of this LMOS phosphor is fixed at around 10 wt.% and the concentration of SiO_2 particles is modifed. This is to influence the scattering performance of the composite to achieve the better color distribution. After sample creation, we analyzed the luminescence of the LMOS in the composite and the effects of the composite with different SiO_2 dosages on the commercial light-emitting diode (LED). When excited via 405-nm ultraviolet, the samples generate red ray under 648 nm matching the shift between $^4G_{5/2}$ and $^6H_{9/2}$ for the ion of Sm^{3+}. With high SiO_2 amounts, the color difference is reduced, and the luminosity is enhanced. The correlated color temperature is also lower, resulting in a warmer white light for the packed LED. However, the color rendering index declines, which could be attributed to the green and blue color deficiency while the red color is dominant. From the tested outcomes, $LiLu(MoO_4)_2:Sm^{3+}@SiO_2$ composite is validated to be effective at improving chromatic uniformity for white-ray diodes.

Keywords: Blue InGaN chips; Color rendering index; Correlated color temperature; White-light-emitting diodes

1. Introduction

Phosphors incorporated with rare-earth ions demonstrate significant utility in the domains of solid-state illumination, solar panels, and heat detectors, owing to their capability to induce diverse transitions involving 4f-4f or 4f-5d energy levels. (Tung, An and Anh, 2023; Yu *et al.*, 2021; Yan *et al.*, 2020). As of today, the fluorescent as well as incandescent outdated lights can be altered in favour of white-light-emitting diodes (WLEDs) because this light source generation offers various qualities including significant performance, low energy consumption, greater durability, etc (Henry and Guruviah, 2020; Kumar *et al.*, 2020; Hansen *et al.*, 2022). These devices are often created by incorporating yellow $YAG:Ce^{3+}$ phosphors and blue InGaN chips. However, this method is deficient in red element within the total spectrum, yielding small color rendering index (CRI) as well as high-level correlated color temperature (CCT) (Bouchakour, Borni, and Brahami, 2021; Finch, Moreno, and Shapiro, 2021; Choi *et al.*, 2019). Red phosphors such as $Y_2O_2S:Eu^{3+}$

*Corresponding author's email: nguyendoanquocanh@tdtu.edu.vn, Tel.: +84-09-66570060
doi: 10.14716/ijtech.v15i1.6165

and CaS:Eu^{2+} lack the efficiency in assimilating within the near-ultraviolet zone. Furthermore, sulfide phosphors degrade after an extensive use, subsequently harming the durability in LED devices. Hence, the exploration and enhancement of new red phosphors capable of producing consistent heat output when stimulated by near-ultraviolet radiation is of paramount importance (Royer *et al.*, 2019; Tian *et al.*, 2019).

Following this, studies placed their aim at creating various phosphors with null heat abatement, including those incorporated with Eu^{2+}, Eu^{3+}, Mn^{2+}, Tb^{3+}, Mn^{4+}, as well as Sm^{3+}. The sample Ca_2InSbO_6:Sm^{3+} yielded null heat abatement when heat level reaches 480 K, an outcome expected for LED devices with significant performance (Guennoun *et al.*, 2021). As such, the task of augmenting phosphors' heat abatement attributes remains particularly difficult when it comes to creating WLED devices based on conversion phosphor. Back to previous eras, various studies were carried out to assess dial molybdates incorporated with rare-earth ions having composition shown as $MLn(MoO_4)_2$ (with M being Li^+, Na^+ and Ln being La^{3+}, Gd^{3+}, Lu^{3+}, Y^{3+}) in the form of inorganic substances, garnering significant notice as they can be diversely utilized for solid-state lasers, scintillators as well as WLED devices (Ranjith *et al.*, 2020; Soltic *et al.*, 2019).

The phosphor bases possessing the $CaMoO_4$ scheelite formation would be assessed through a unique disarrangement for the surroundings for the ions of RE^{3+} with the Ca^{2+} locations from $CaMoO_4$ contingently inhabited by half of the alkali metal ion M^+ as well as half of the rare earth ion Ln^{3+} (Attanayake, Okuya, and Murakami, 2020). Dual molybdate blends typically possess wide, potent charge shift line within the near-ultraviolet zone as well as desirable heat consistency, proving to be a fitting base substance that can be diversely utilized for WLED devices incorporated with rare-earth phosphors (Praveen *et al.*, 2021; Königs, Mayr, and Buchner, 2019). The ions of Sm^{3+} would be a typical trigger for orange-red discharge as it has shifts between $^4G_{5/2}$ and ^6H_J with J as 5/2, 7/2, 9/2, 11/2, being the best source when it comes illumination and exhibition (Astuti *et al.*, 2020). In addition, certain phosphors incorporated with Sm^{3+} were created and utilized for WLED at some points in the past. The $LiLu(MoO_4)_2$:Sm^{3+} (LMOS) phosphor created with sol-gel method could provide red-light component for the WLED's spectrum, which is supposed to effectively improve the chromatic rendition of the package (Irawan *et al.*, 2020). However, this phosphor performance is barely investigated for conventional white LED with blue InGaN chips. Therefore, in this work, the LMOS phosphor is utilized for the goal of improving color uniformity and light distribution of the conventional LED device. This work creates a phosphor composite comprising the LMOS red phosphor, YAG:Ce^{3+} yellow phosphor, SiO_2 scattering improvement particles, and silicone gel, called LMOS@SiO_2 hereafter. This composite is applied for the white LED with blue InGaN chips. In this composite, we adjust the doping dosage of SiO_2 while keeping the dosage of LMOS phosphor constant. This is to regulate the lighting performance of the WLED with LMOS@SiO_2 via the light-scattering modification. Judging the outcomes, LMOS@SiO_2 composite proves to be useful for reducing color deviation level while improving luminosity for the WLED device.

2. Methods

2.1. Creating LMOS phosphors

The LMOS samples were created using the sol-gel procedure. The ingredients used for the procedure were obtained in a pure, uncontaminated form. Table 1 lists said ingredients along with the procedure's steps, which also apply to $LiLu_{(1-x)}(MoO_4)_2$:x% Sm^{3+} with x values of 0.5, 1, 3, 5, 7, 10 (Winberg-Wang, 2019).

Table 1 Ingredients and steps to create LMOS

Ingredients	Steps
Lu_2O_3 Sm_2O_3 Li_2CO_3 $(NH_4)_6Mo_7O_{24}.4H_2O$ $C_6H_8O_7{\cdot}H_2O$ HNO_3	- First, we dissolve Lu_2O_3 as well as Sm_2O_3 using dilute nitric acid to get the rare-earth nitrates. - Next, Li_2CO_3 is incorporated to the said nitrates to form a new compound, called compound 1 herein. - Then, we dissolve $(NH_4)_6Mo_7O_{24}.4H_2O$ along with $C_6H_8O_7{\cdot}H_2O$ (in the form of chelating substance) with proportion between citric acid and metal ion as 2:1 using deionized H_2O to get a solution called compound 2. - The compound 2 is subsequently added to compound 1 and the new mixture is created. The pH of this new mixture is fixated to 6 using $NH_3{\cdot}H_2O$. - Continuously, a heating and then stirring process under 353 K is carried out for the mixture to create a dry gel in yellow. - To get the final product from the attained gel, we pulverize the gel within agate mortal, then calcine it within a muffle furnace under 973 K within five hours. The obtained phosphor substances yield white hue.
$NH_3{\cdot}H_2O$	

2.2. Assessing attributes

Following the creation of the samples, assessments were carried out to determine their attributes. Appropriate tools were utilized for this task. Table 2 below details attributes along the tools used (Altenberg-Vaz and Inanici., 2021).

Table 2 Attributes and associated tools used for the samples

Attributes	Assessing tools
Stage data	X-ray powder diffraction (XRD) via Panalytical X'Pert diffractometer with Cu-$K_{\alpha1}$ (λ = 0.154187 nm) radioactivity within the scanning scope of 2θ = 10–80 ◦ at scanning rate reaching 10 ◦ each minute
Rietveld formation rectification	Smart Lab Studio II program
Form	Field discharge scanning electron microscope (SEM JSM-6700F) accompanied by power-dispersal spectrometer spectra
Ultraviolet–observable dispersal reflectance spectrum along with Fourier Infrared spectrum	UV-2500 UV–Vis spectrophotometer along with ALPHA infrared spectrometer
Photoluminescent spectra as well as luminescent degradation arches based on heat level	Fluorolog-3 fluorescent spectrometer (Fluorolog-3, Jobin Yvon, USA)

3. Results and Discussion

3.1. Luminescence calculation for LMOS

The power gap will be determined via ultraviolet-observable absorbing spectra by applying the expression below (equation 1) (Nahon, Beckers, and Blanpain, 2019):

$$ahv = K\left(hv - E_g\right)^n \quad (1)$$

α signifies the absorptivity coefficient. h signifies Planck constant. v signifies optical periodicity. K signifies constant. n signifies constant corresponding to various forms of electron shifts with values of 1/2, 2, 3/2, 3 respectively applying to directly allowed, indirectly allowed, directly forbidden, indirectly forbidden shifts.

For the task of generating non-radioactive power shift among the surrounding Sm^{3+} triggers, two distinct forms of non-radioactive power shift exist: reciprocating interactivity as well as multi-state interactivity. Assessing the critical range would be necessary to identify the best one. Power shift via multi-polar interactivity manifests if the critical range exceeds 5 Å. On the other hand, reciprocating interactivities manifest if critical range goes

below 5 Å. For the task of clarifying the concentration abatement, the critical range will be determined by the expression below (equation 2) (Ali *et al.*, 2019):

$$R_C = 2[\frac{3V}{4\pi_{\chi_c} N}]^{\frac{1}{3}} \quad (2)$$

V signifies cell's volume as 289.854 Å. χ_c signifies the critical concentration. N signifies the cation amount within the latticework, equal to 2. The yielded critical range reaches 20.974 Å, noticeably exceeding 5 Å. As such, the non-radioactive power shift would be deemed multi-polar interactivity. Based on Dexter's work, it is possible to utilize an expression for the task of approximating the potential forms of said interactivity (equation 3) (Pierson *et al.*, 2021):

$$\frac{I}{x} = \frac{K}{1+\beta x^{\frac{\theta}{3}}} \quad (3)$$

The CIE coordinates for LMOS when excited at 405 nm appeared to be (0.5806, 0.4145), resulting in the display of red discharge within the hue scale. For the task of illustrating the capabilities for LMOS, we assessed the sample's correlated color temperature (CCT) as well as hue clarity. The McCamy expression below will determine the CCT (equation 4) (Chen and Wu, 2019):

$$-449n^3 + 3525n^2 - 6823n + 5520.33 \quad (4)$$
$$n = \frac{(x - x_e)}{y - y_e}$$

x_e (0.03320) and y_e (0.1858) denote hue focal points with x, y being the CIE coordinates. The yielded correlated color temperature output reached 1692.08. The hue clarity would be essential for the task of assessing the luminescent output for LMOS and will be determined via the expression below (equation 5) (Xue and Xie, 2020):

$$\frac{\sqrt{(x-x_i)^2+(y-y_i)^2}}{\sqrt{(x_d-x_i)^2+(y_d-y_i)^2}} \quad (5)$$

The yielded hue clarity reached 98.94% with hue coordinates (x, y) for LMOS as (0.5806, 0.4145), the white illuminating site (x_i, y_i) as (0.3333, 0.3333), as well as prevalent wavelength site (x_d, y_d) as (0.5834, 0.4158).

It is possible to fit the luminescent degradation arch by utilizing dual-exponential expression (equation 6) (Mukunda, Joshi, and Mahato, 2022):

$$I(t) = I_0 + A_1 \exp(-t/\tau_1) + A_2 \exp(-t/\tau_2) \quad (6)$$

I(t) signifies the discharge intenseness under time t. I_0 signifies the surrounding's intenseness. A_1, A_2 signify fitting constants. τ_1, τ_2 signify the rapid and slow elements for the degradation arch. The expression below will determine the median durations (equation 7) (Eisazadeh, Allacker, and Troyer, 2021):

$$\tau_{av} = (A_1\tau_1^2 + A_1\tau_2^2)/(A_1\tau_1 + A_1\tau_2) \quad (7)$$

3.2. LMOS@SiO_2 effects on WLED outputs as a function of varying SiO_2 amounts

In the prepared composite, the concentration of YAG:Ce^{3+} phosphor must be changed corresponding to different doping amount of the SiO_2 particles. This situation is demonstrated in Figure 1. In the graph, the amount of SiO_2 varies from 0 wt.% to 50 wt.%, followed by the decline in YAG:Ce^{3+} concentration. Particularly, these changes appear to be an inverse mechanism, with the YAG:Ce amount almost linearly decreasing from its peak at 0 wt.% SiO_2 to the bottom at 50 wt.% SiO_2. As the amount of SiO_2 surges, the scattering coefficient is heightened, leading to better dispersion for the illumination. Besides, the generated light by blue chip can be effectively propagated then transmitted through the phosphor composite. As a result, the amount of re-absorbed light by phosphors is reduced, the luminescence will be heightened when the blue-ray dispersion in the direct path surges

while the blue-ray rear-dispersion is diminished (Rubeis *et al.*, 2021). So, the decreasing concentration of YAG:Ce^{3+} phosphor contributes to improving the scattering performance in the presence of increasing SiO_2 dosage.

With the enhancing scattering performance, higher SiO_2 dosages also affect correlated color temperature (CCT) levels, as shown in Figure 2. In the figure, the CCT levels recorded in the viewing angles of ±90° with SiO_2 amounts range of 0-50 wt.%. In general, in ±20°, the CCT level declines and becomes relatively flattened as we increase the SiO_2 concentration. This indicates that the white light is warmer when exposing to human eyes directly. On the other hand, in ±90°, the CCT levels exhibit a significant fluctuation, but still lower than the value obtained with 0 wt.% SiO_2 in the package. The deviation of CCT range is particularly calculated and displayed in Figure 3. Apparently, with different SiO_2 dosages, the CCT show notable fluctuations. However, as the SiO_2 amount increases continuously to 50 wt.%, significant CCT-deviation reduction is achieved. The CCT is at its lowest with the SiO_2 amount of 50 wt.%. The other notable CCT-deviation reduction levels are also obtained with SiO_2 concentration of 30-35 wt.%. Though with the amount of 40-45 wt.% SiO_2, the CCT-level aberration sharply goes up, it is lower than the CCT level of the composite sample without SiO_2. This indicates that the light dispersion is influenced and enhanced with the presence of SiO_2, revealing the enhancement in converted red-light proportion by LMOS phosphor.

Conversely, for the lumen of the WLED shown in Figure 5, the considerable and continuous rise is noticed regarding the higher SiO_2 doping amounts. This event could be a result from the better blue-light discharge induced by greater forward light dispersion and lower light re-absorbance. It is noteworthy that increasing the particle concentration of SiO_2 can enhance the transformation of illumination from blue to yellow or red-orange. This effect is primarily attributed to the broader scattering range, allowing more blue light to be mixed, to interact with the phosphor particles in the composite, and be converted. However, if the scattering is too much, the transformed light may undergo rear-reflection, thereby possibly reducing the intensity of luminescence and resulting in a higher correlated color temperature (CCT) level (Costa *et al.*, 2019). Thus, we predict that if the SiO_2 is more than 50 wt.%, the luminous flux of the WLED with LMOS@SiO_2 sheet will decline. Yet, this will be analyzed in future works.

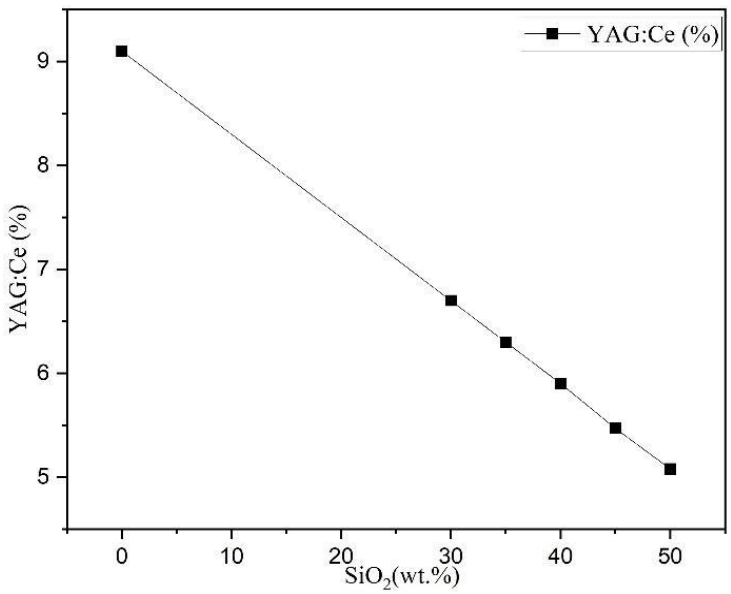

Figure 1 YAG:Ce concentration under influence of increasing SiO_2 amount

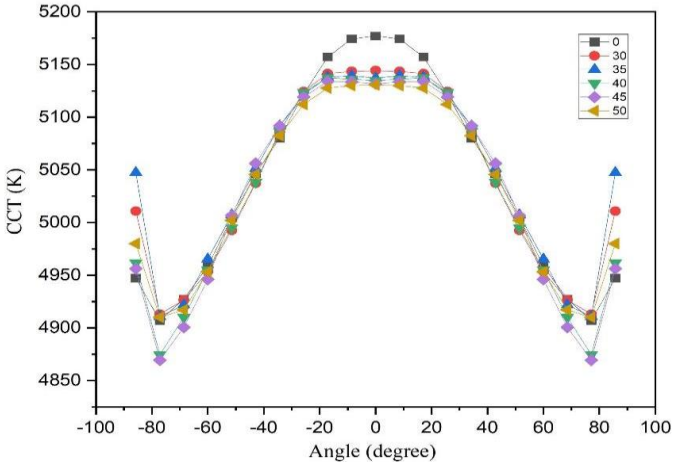

Figure 2 Angular CCT range monitored with different SiO_2 amounts

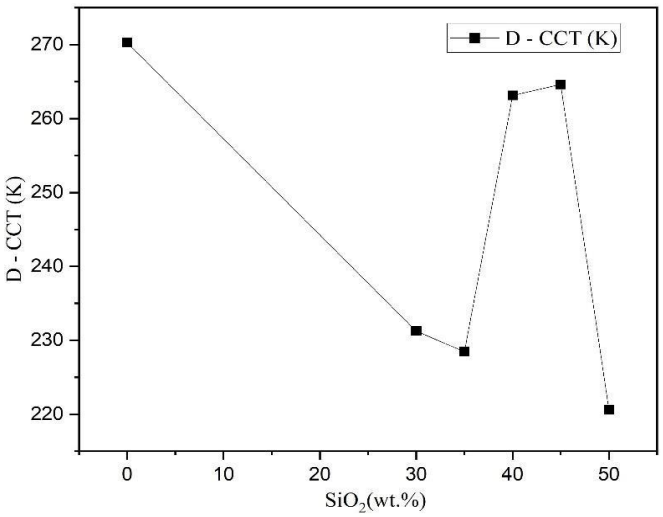

Figure 3 CCT-range deviation responding to different SiO_2 amounts

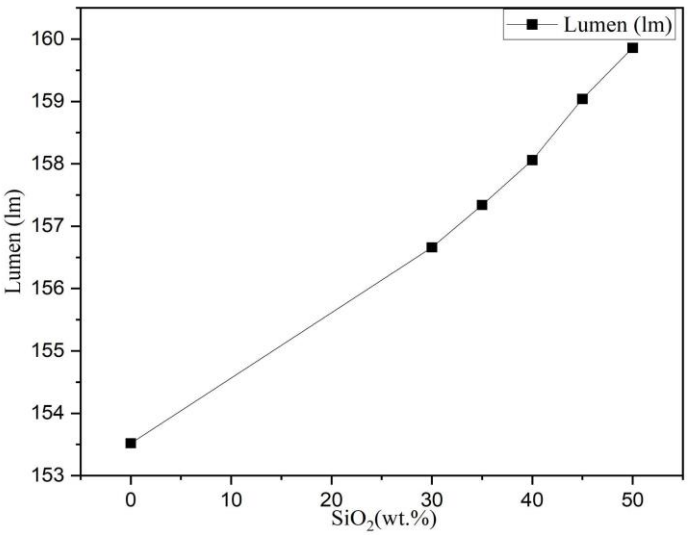

Figure 4 LED lumen responding to different SiO_2 amounts

The output of hue generation of the WLED device is also affected by the dosage of SiO_2. As the particle size increases from 0 wt.% to 50 wt.%, color rendering index (CRI) and color quality scale (CQS) shows a noticeable deterioration in a relatively linear manner, see

Figures 5 and 6, respectively. This observed decline is possibly the result of the lack of green and blue spectra in the white light emission. Under great dosages of SiO_2, the heightened dispersion generates more orange-yellow elements, resulting in the mentioned emission-color deficiency since the ray's discharge hue generally favors the orange-yellow zone. As such, unnecessary dispersion can cause inferior CRI as well as CQS (Guerra *et al.*, 2020).

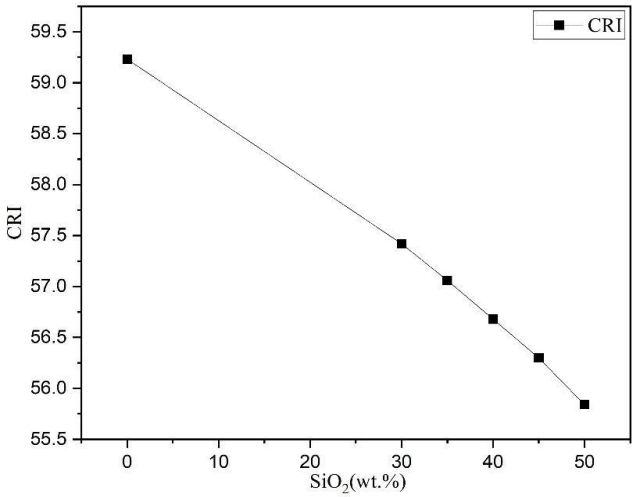

Figure 5 CRI under influence of SiO_2 particle size

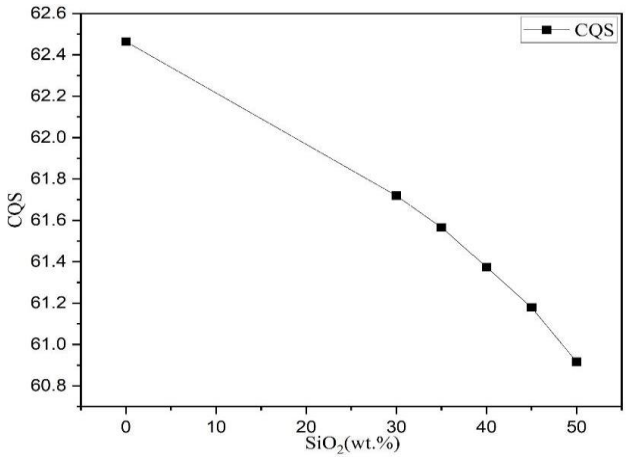

Figure 6 CQS under influence of SiO_2 particle size

In the previous eras where the scientific fields were unfamiliar with hue assessment, color rendering index (CRI) was created and was deemed the only way to evaluate the quality of hue generation in a ray when compared to natural lights. Eventually, the flaws of CRI became a concern (Danny *et al.*, 2020). Notably, its mechanism to measure hue desirability in lighting devices was not reliable for utilizing outdated hue samples and inaccurate hue scale. In the case of incandescent lights with perfect CRI output of 100, it was reported that the human sight did not witness the correct hue recreation based on the standard of sun ray (Thi *et al.*, 2023). For fluorescent light which yielded a low CRI output, its ability to illuminate the environment was found to be superior. When it comes to LED devices, they generate desirable light while not generating significant temperature, a factor that is heavily assessed by CRI considering that luminescent light was unheard of back in the old times. As a result, high-quality WLED devices end up yielding an inferior CRI when compared to the more outdated lights mentioned above. Color quality scale (CQS), on the other hand, overcome the drawbacks of its predecessor by assessing more facets, such as human preference as well as additional hue samples, thus yielding more accurate results

that fit our perception and proven to be a better hue-output indicator for WLED devices (Thai *et al.*, 2023).

4. Conclusions

The study herein concerns phosphor $LiLu(MoO_4)_2:Sm^{3+}@SiO_2$ composite for the conventional WLED model with blue chips. The LMOS phosphor possesses the tetragonal setting and generates red ray under 648 nm when excited via near-ultraviolet ray under 405 nm. The primary concentration abatement nature in Sm^{3+} appeared to be the result of dipole-dipole interactivities. By fixing the concentration of LMOS phosphor and varying the SiO_2 doping amount, the illumination properties including color distribution and luminosity of the WLED can be regulated. Specifically, increasing the SiO_2 content leads to a decrease in color discrepancy and an improvement in brightness. Additionally, it results in a lower correlated color temperature, creating a warmer white light for the compact LED. However, this increase in SiO_2 content also causes a decline in the color rendering index, which can be attributed to a deficiency in green and blue colors while the red color remains dominant. The outcomes prove that $LiLu(MoO_4)_2:Sm^{3+}@SiO_2$ can be used to generate red rays and induce color uniformity for conventional WLED devices.

References

Altenberg-Vaz, N., Inanici, M., 2021. Syncing with the Sky: Daylight-Driven Circadian Lighting Design. *LEUKOS (The Journal of the Illuminating Engineering Society*), Volume 17, pp. 291–309

Astuti, Y., Amri, D., Widodo, D.S., Widiyandari, H., Balgis, R., Ogi, T., 2020. Effect of Fuels on the Physicochemical Properties and Photocatalytic Activity of Bismuth Oxide, Synthesized using Solution Combustion Method*. International Journal of Technology,* Volume 11(1), pp. 26–36

Attanayake, S., Okuya, M., Murakami, K., 2020. Spray Angle Dependence for the Growth of Terrace-truncated Nanocone Structure of Gallium-doped Zinc Oxide by Advanced Spray Pyrolysis Deposition Technique. *International Journal of Technology*, Volume 11(1), pp. 81–90

Beattie, J.R., Esmonde-White, F.W.L., 2021. Exploration of Principal Component Analysis: Deriving Principal Component Analysis Visually Using Spectra. *Applied Spectroscopy,* Volume 75, pp. 361–375

Bouchakour, A., Borni, A., Brahami, M., 2021. Comparative Study of P&O-PI and Fuzzy-PI MPPT Controllers and Their Optimisation Using GA and PSO For Photovoltaic Water Pumping Systems. *International Journal of Ambient Energy*, Volume 42, pp. 1746–1757

Chen, H., Wu, S., 2019. Advanced Liquid Crystal Displays with Supreme Image Qualities. *Liquid Crystals Today*, Volume 28, pp. 4–11

Choi, H., Huh, D., Jun, J., Lee, H., 2019. A Review on the Fabrication and Applications of Sub-Wavelength Anti-Reflective Surfaces Based on Biomimetics. *Applied Spectroscopy Reviews*, Volume 54, pp. 719–735

Costa, J.A., Brito, J., Nakamura, F.Y., Figueiredo, P., Oliveira E., Rebelo, A., 2019. Sleep Patterns and Nocturnal Cardiac Autonomic Activity in Female Athletes Are Affected by The Timing of Exercise and Match Location. *Chronobiology International*, Volume 36(3), pp. 360–373

Danny, S.C.N, Fung, N.S.K., Yip, F.L.T., Lai, T.Y.Y., 2020. Ranibizumab For Myopic Choroidal Neovascularization. *Expert Opinion on Biological Therapy*, Volume 20, pp. 1385–1393

Eisazadeh, N., Allacker K., Troyer, F.D., 2021. Integrated Energy, Daylighting and Visual Comfort Analysis of Window Systems in Patient Rooms. *Science and Technology for the Built Environment*, Volume 27, pp. 1040–1055

Finch, L., Moreno, C., Shapiro, R.B., 2021. Luminous Science: Teachers Designing For and Developing Transdisciplinary Thinking and Learning, *Cognition and Instruction*, Volume 39, pp. 512–560

Guennoun, A., Marsi, M.E., Fechtal, I., Elhaitamy, O., Dezairi, A., 2021. Noble Gas Ion Beam Bombardment Effects on H-, graphite -, Na-, Fe- and Zn-doped MgO Thin Films in Plasma-Related Discharge Devices. *Molecular Crystals and Liquid Crystals*, Volume 722, pp. 76–86

Guerra, A.P., Bermejo, S.P., Prieto, L.F.C., Llorente, M.S., 2020. Environmental Impact Study of Symphony Orchestras and Preparation of a Classification Guide. *International Journal of Environmental Studies*, Volume 77, pp. 1044–1059

Hansen, E.K., Pajuste, M., Xylakis, E., 2022. Flow of Light: Balancing Directionality and CCT in the Office Environment. *LEUKOS (The Journal of the Illuminating Engineering Society*), Volume 18, pp. 30–51

Henry, R., Guruviah, V., 2020. Thermal Analysis of Light Source for Optogenetics Experiments. *IETE Journal of Research*, Volume 66, pp. 270–285

Irawan, B., Darmawan, A., Roesyadi, A., Hari Prajitno, D., 2020. Improving Reaction Selectivity with NaOH Charges and Reaction Time in the Medium Consistency Oxygen Delignification Process. *International Journal of Technology*, Volume 11, pp. 764–773

Königs, S., Mayr, S., Buchner, A., 2019. A Common Type of Commercially Available LED Light Source Allows For Color Discrimination Performance At A Level Comparable To Halogen Lighting. *Ergonomics*, Volume 62, pp. 1462–1473

Kumar, S., Prince, S., Aravind, J.V., Kumar, GS., 2020. Analysis on The Effect Of Salinity In Underwater Wireless Optical Communication. *Marine Georesources & Geotechnology*, Volume 38, pp. 291–301

Mukunda, D.C., Joshi, V.K., Mahato, K.K., 2022. Light Emitting Diodes (LEDs) In Fluorescence-Based Analytical Applications: A Review. *Applied Spectroscopy Reviews*, Volume 57, pp. 1–38

Nahon, R., Beckers, B., Blanpain, O., 2019. Evaluation of The Daylight Conditions at Early Stages of an Urban Project. *European Journal of Environmental and Civil Engineering*, Volume 23, pp. 728–742

Pierson, C., Cauwerts, C., Bodart, M., Wienold, J., 2021. Tutorial: Luminance Maps for Daylighting Studies from High Dynamic Range Photography. *LEUKOS (The Journal of the Illuminating Engineering Society*), Volume 17, pp. 140–169

Praveen, A.S., Jithin, R., Kumar, K.N., Baby, M., 2021. Analysis of Thermal and Optical Characteristics of Light-Emitting Diode on Various Heat Sinks. *International Journal of Ambient Energy*, Volume 42, pp. 854–859

Ranjith, P., Manimaran, A., Praveen, A.S., Ramesh, T., 2020. Experimental Investigation of Heat Transfer Characteristics of the LED Module Using Passive Heat Sinks. *International Journal of Ambient Energy,* Volume 41, pp. 1209–1213

Royer, M., 2019. Evaluating Tradeoffs Between Energy Efficiency and Color Rendition, *OSA Continuum,* Volume 2, pp. 2308–2327

Rubeis, T.D., Smarra, F., Gentile, N., D'innocenzo, A., Ambrosini, D., Paoletti, D., 2021. Learning Lighting Models for Optimal Control Of Lighting System Via Experimental and Numerical Approach. *Science and Technology for the Built Environment*, Volume 27, pp. 1018–1030

Soltic, S., Chalmers, A.N., 2019. Prospects For 4-Laser White-Light Sources. *Journal of Modern Optics*, Volume 66, pp. 271–280

Thai, N.L., Bui, T.M., Le, A.T., Thi, D.A.N., 2023. Utilization of $BaAl_{1.4}Si_{0.6}O_{3.4}N_{0.6}:Eu^{2+}$ Green-emitting Phosphor to Improve Luminous Intensity and Color Adequacy of White Light-emitting Diodes. *International Journal of Technology*, Volume 14(1), pp. 119–128

Thi, M.H.N., Thai, N.L., Bui, T.M., Thao, N.T.P., 2023. $Ca_8MgY(PO_4)_7:Eu^{2+},Mn^{2+}$: A Promising Phosphor in Near-Ultraviolet WLED Devices. *International Journal of Technology*. Volume 14(3), pp. 501–509

Tian, Y., Tang, Y., Yi, X., Chen, J., Ao, G., Hao, D., Lin, Y., Zhou, S., 2019. Study of composite Al_2O_3-Ce:$Y_3Mg_{1.8}Al_{1.4}Si_{1.8}O_{12}$ Ceramic Phosphors. *Optics Letters,* Volume 44(19), pp. 4845–4848

Tung, H.T, An, N.T.D., Anh, N.D.Q., 2023. The effects of $Ca_{14}Mg_2(SiO_4)_8:Eu^{2+}$ Phosphor on white Light Emission Quality of LED-Phosphor Packages. *Bulletin of Electrical Engineering and Informatics,* Volume 12(6), pp. 3388–3394

Winberg-Wang, H., Neretnieks, I., Voutilainen, M., 2019. A Note on the Use of Uranine Tracer to Visualize Radionuclide Migration Experiments: Some Observations and Problems. *Nuclear Technology*, Volume 205, pp. 964–977

Xue, Q., Xie, G., 2020. Easily Reproducible Top-Emitting Organic Light-Emitting Devices for Microdisplays Adapted to Aluminum Contact from The Standard CMOS Processes. *Journal of Information Display*, Volume 21, pp. 131–137

Yan, D., Zhao, S., Wang, H., Zang, Z., 2020. Ultrapure And Highly Efficient Green Light Emitting Devices Based on Ligand-Modified $CsPbBr_3$ Quantum Dots. *Photonics Research,* Volume 8(7), pp. 1086–1092

Yu, Z., Yang, J., Lin, C., Zhang, X., Dang, F., Yuan, Y., Yuan, L., Wang, Y., Qin, Y., 2021. Distributed Polarization Measurement for Fiber Sensing Coils: A Review. *Journal of Lightwave Technology,* Volume 39(12), pp. 3699–3710